The Lamellar Structure of the Brain Fiber Pathways

Vitaly L. Galinsky

vit@ucsd.edu

Center for Scientific Computation in Imaging and Electrical and Computer Engineering Department, University of California at San Diego, La Jolla, CA 92093, U.S.A.

Lawrence R. Frank

lfrank@ucsd.edu

Center for Scientific Computation in Imaging and Department of Radiology, University of California at San Diego, La Jolla, CA 92093, U.S.A., and VA San Diego Healthcare System, San Diego, CA 92093, U.S.A.

We present a quantitative statistical analysis of pairwise crossings for all fibers obtained from whole brain tractography that confirms with high confidence that the brain grid theory (Wedeen et al., 2012a) is not supported by the evidence. The overall fiber tracts structure appears to be more consistent with small angle treelike branching of tracts rather than with near-orthogonal gridlike crossing of fiber sheets. The analysis uses our new method for high-resolution whole brain tractography that is capable of resolving fibers crossing of less than 10 degrees and correctly following a continuous angular distribution of fibers even when the individual fiber directions are not resolved. This analysis also allows us to demonstrate that the whole brain fiber pathway system is very well approximated by a lamellar vector field, providing a concise and quantitative mathematical characterization of the structural connectivity of the human brain.

1 Introduction ____

Advances in modern digital imaging methods are revolutionizing a wide range of scientific disciplines. One of these truly revolutionary approaches that has become ubiquitous in basic neuroscience research and has the potential to have significant impact on a wide range of clinical applications is the noninvasive reconstruction of neural tissue fiber pathways from volumetric diffusion tensor magnetic resonance imaging (DTI) data. The basic DTI procedure is to collect multiple image volumes (a Cartesian sampling of image space), each with a different combination of the magnitude and direction of the diffusion sensitivity. The standard procedure for analyzing these data is to reconstruct the local (i.e., voxel) diffusion profile from this

sampling of diffusion sensitivity, or *q*, space, then estimate global measures of connectivity (tracts) by constructing relationships between the diffusion profiles in each voxel in the Cartesian image space, typically by generating streamlines through the angular maxima of the voxel-derived diffusion profiles, or probability density functions (PDFs).

Wedeen et al. (2012a) used a variant of the DTI protocol, diffusion spectrum imaging (DSI), to develop a theory that white matter fibers form a regular grid by crossing almost orthogonally and uniformly in the entire brain. The DSI protocol performs a Cartesian sampling of *q*-space, then estimates the average diffusion propagator locally (in each voxel), and finally extracts the orientation distribution function (ODF), the radial average PDF (Tuch et al., 2002), again in each voxel. This locally estimated ODF is used to guide the global fiber tractography (Conturo et al., 1999; Basser, Pajevic, Pierpaoli, Duda, & Aldroubi, 2000; Mori & van Zijl, 2002; Jbabdi & Johansen-Berg, 2011), which implicitly assumes that all the information about the crossing of fibers can be extracted from this local ODF. A significant and overly simplistic assumption that is made is that an ODF with a single lobe describes a unidirectional set of fibers, whereas an ODF with multiple lobes possessing relatively similar amplitudes is assumed to represent multiple fiber orientations.

The grid theory was criticized by Catani, Bodi, and Dell'Acqua (2012) who used whole brain streamline tractography based on a different local diffusion profile estimation technique, the spherical deconvolution (SD), which has been demonstrated to consistently resolve fiber crossings above at least 45 degrees (Tournier, Calamante, & Connelly, 2007). Their results show the distribution of the angles of fiber crossing in a sample of 10 healthy human brains and demonstrate the high probability of nonorthogonal fiber crossings in the human brain, with nonorthogonal crossings at least as likely (and probably more likely) as orthogonal crossings, which were shown to account for less than 12% of the total crossings in the human white matter. Their conclusion is that the grid pattern Wedeen observed is most likely an artifact attributable to the limitations of the DSI approach, which has low angular resolution and thus preferentially detects orthogonal crossings since streamlines through nonorthogonal fibers stop in the deep white matter. This is probably due to a limitation of the majority of deterministic tracking approaches that not only prohibit sharp fiber turns but typically impose explicit or implicit stopping criteria to avoid tracking through low anisotropy regions. The result is that the appearance of the vast majority of fiber crossing appears to be orthogonal.

In the response to Catani's criticism, Wedeen et al. (2012b) claim that their DSI acquisition has higher spatial or diffusion resolution (or both) and therefore is able to detect many areas where the fiber tracts exhibit very sharp changes of direction. Hence, the current MRI tractography that relies on orientation continuity (i.e., requires path curvature of 1 rad/voxel or lesss) (Wedeen et al., 2008) is the culprit of those artifactual trajectories,

as it is unable to continue paths through those areas and instead shows terminations of corticospinal paths where they should be turning sharply. Moreover, it is claimed that the Cartesian *q*-space sampling used in their implementation of DSI presents a lower risk of bias and is thus a more conservative choice of methods when microstructure is uncertain (Wedeen et al., 2012b). More recently, in a sequence of workshop presentations (Tax et al., 2013, 2014, 2015, Tax, Haije et al., 2016), several quantitative techniques were attempted to evaluate the existence of sheet structure, but no convincing arguments were provided.

In this letter, we present a quantitative statistical analysis of pairwise crossings for all fibers obtained from whole brain tractography that confirms with high confidence that the brain grid theory is not supported by the evidence. The analysis uses our new method for high-resolution whole brain tractography that is capable of resolving fibers crossing of less than 10 degrees. This analysis also allows us to demonstrate that the whole brain fiber pathway system is well approximated by a lamellar vector field, providing a concise and quantitative mathematical characterization of the structural connectivity of the human brain.

2 Method _

In an attempt to resolve the brain grid theory controversy, we conducted a high-resolution tractography study using our recently developed (Frank & Galinsky, 2014; Galinsky & Frank, 2015) geometrical optics-guided entropy spectrum pathways (GO-ESP) fiber tracking method (the details of our tracking approach can be found in (Galinsky & Frank, 2015). The GO-ESP method performs a simultaneous estimation of the local diffusion profile and the global structure of the fiber pathways by the use of prior information on local coupling within a fully Bayesian probabilistic framework. Thus, in a formal probabilistic sense, it is the most conservative approach to the inverse problem of determining fiber pathways from diffusion-weighted MRI signals. Moreover, because the GO-ESP tracking approach is based on geometrical optics, it does not introduce limits on paths curvature, and in certain circumstances should theoretically be able to detect nearly complete path reversals (approximately 180 degrees), in a manner similar to those found in optical reflection. Hence it is able to detect and proceed though the sharp turns reported by Wedeen et al. (2012b). More important, the GO-ESP approach does not rely on the locally inferred ODF and does not make any assumptions about the number of crossing fibers present in each voxel. Instead, we assume a continuous distribution of fiber directions and derive an equation to update the fiber orientation at each tracking step in a globally consistent way. Hence, we trace both fiber position r and fiber orientation k simultaneously by solving two equations of Hamilton-Jacobi type at each step (Galinsky & Frank, 2015),

$$\frac{d\mathbf{r}}{dt} = \frac{\partial \mathcal{H}}{\partial \mathbf{k}} \equiv \psi(\mathbf{r}, \mathbf{k}), \qquad \frac{d\mathbf{k}}{dt} = -\frac{\partial \mathcal{H}}{\partial \mathbf{r}} \equiv \xi(\mathbf{r}, \mathbf{k}), \tag{2.1}$$

where \mathcal{H} is the Hamiltonian that can be expressed through equilibrium and transitional probabilities using the entropy spectrum pathways procedure (Frank & Galinsky, 2014). The traditional fiber tracking approach defines tracts by integration of position—only function ψ , which assigns the tangential direction of tracts to each location r. For our geometrical optics GO-ESP approach, the integration takes into account both the orientation and multiple scales, through the dependence of ψ on directional angle k/|k| and magnitude |k|. (The details about functions ψ and ξ can be found in Galinsky & Frank, 2015.)

For whole brain tractography, we used one of the publicly accessible diffusion imaging data sets (MGH 1010) available from the Human Connectome Project (Van Essen et al., 2012; Sotiropoulos et al., 2013), as well as several diffusion imaging data sets collected locally.

The HCP MGH 1010 data set was collected on the customized Siemens 3T Connectom scanner, a modified 3T Skyra system (MAGNETOM Skyra Siemens Healthcare), housed at the MGH/HST Athinoula A. Martinos Center for Biomedical Imaging (see Setsompop et al., 2013, for details of the scanner design and implementation). A 64-channel, tight-fitting brain array coil (Keil et al., 2013) was used for data acquisition. The data set contains 96 slices of 140×140 matrix (1.5 mm linear voxel size) at four levels of diffusion sensitizations (b-values b = 1k, 3k, 5k, and 10k s/mm²) distributed over 552 total q-vectors.

The local data were collected by the UCSD Center for Functional MRI (CFMRI) using the 3T GE Discovery MR750 whole body system. The anatomical T1 volumes have $168 \times 256 \times 256$ voxel size with $1.2 \times 0.9375 \times 0.9375$ mm³ resolution. A multiband DTI EPI acquisition (Setsompop et al., 2011) using three simultaneous slice excitations was used to acquire data with three diffusion sensitizations (at b-values: $b = 1000/2000/3000 \, \text{s/mm}^2$) for 30, 45, and 65 different diffusion gradients (respectively) uniformly distributed over a unit sphere. Several baseline (b = 0) images were also recorded. The data were reconstructed offline using the CFMRI's multiband reconstruction routines. The DWI data sets have $100 \times 100 \times 72$ voxel size with $2 \times 2 \times 2$ mm³ resolution.

The spherical multishell encoding is different from the DSI Cartesian q-space sampling of Wedeen et al. (2012a), but with 552 q-vectors, it provides better angular (diffusion) resolution than DSI sampling with 515 q-vectors distributed inside the sphere of radius 5. Both acquisition schemes have a comparable number of diffusion sampling directions, but in our acquisition, the diffusion sensitization weighted distribution of q-vector directions (i.e., the distribution with a different number of points more or less uniformly distributed at each diffusion sensitization level) is optimized to provide a more accurate sampling of the angular diffusion variations than an

equidistant Cartesian grid. Indeed, the DSI Cartesian q-space sampling has roughly a similar number of points at the highest sensitization levels (256 for multishell versus 258 for DSI) providing 0.0487 steradian resolution (versus 0.0491 sr for multishell), but at the lowest sensitizations, multishell sampling with 64 points still has reasonably accurate 0.196 sr resolution, whereas the DSI sampling falls to 2.09 sr resolution, which is only able to resolve directions that are fairly close to orthogonal. A simple estimate for mean angular resolution of DSI sampling with 515 grid points distributed inside the sphere of radius 5 is

$$\overline{\Delta\Omega}_{DSI} = \frac{1}{5-1} \int_{1}^{5} \left(\frac{5}{r}\right)^{3} \frac{4\pi}{515} dr = 0.366 \text{ sr},$$
 (2.2)

whereas for 64, 64, 128, and 256 points multishell aquisition, it is

$$\overline{\Delta\Omega}_{MS} = \frac{4\pi}{4} \left(\frac{1}{64} + \frac{1}{64} + \frac{1}{128} + \frac{1}{256} \right) = 0.135 \text{ sr} \lesssim 0.5 \overline{\Delta\Omega}_{DSI}, \quad (2.3)$$

that is, more than twice as better.

It is important to point out at this juncture that a key result of our analysis leading to the GO-ESP method (Galinsky & Frank, 2015) is that the generally accepted view that the diffusion PDF is the fundamental quantity in diffusion MRI methods is predicated on the assumption that voxel diffusion profiles are independent. Although there are currently methods that introduce bridging for the local and global scales, (i.e. through spatially regularized ODF reconstruction; Goh, Lenglet, Thompson, & Vidal, 2009; Reisert et al., 2011), or by augmenting streamline tractography with some pseudo-global-looking schemes (Kreher et al., 2008; Fillard, Poupon, & Mangin, 2009; Reisert, Kiselev, Dihtal, Kellner, & Novikov, 2014; Christiaens et al., 2015), the majority of these methods perform diffusion estimation and tractography independently. The fact that voxel diffusion profiles measured in diffusion-weighted images of continuous underlying white matter structures are clearly not independent leads to the logically inconsistent procedures whereby local diffusion is estimated based on this assumption of independence, whereas tractography is constructed based on the implicit assumption of dependence. Our probabilistic approach incorporates additional prior information about nearest-neighbor coupling, and in this case, the result is that the fundamental quantity is not the PDF but the transition probability for information flow between different voxels. Consequently, methods that hold to the view that the PDF is the fundamental quantity are thus limited not by the acquisition, but by the problem formulation used in the analysis. Conversely, the GO-ESP method is capable of resolving a huge number of fiber crossings at very small angular difference

from multishell diffusion acquisitions now easily attainable on state-of-theart scanners (Galinsky & Frank, 2015).

We emphasize that the use of the term fiber is a primary source of confusion in DTI. Current MRI technology is not able to resolve individual fibers and samples them only statistically. Typical neural fibers can differ in diameter by nearly 100-fold (approximately 0.1–10 μ m); hence, one would need between 10⁵ and 10⁹ total fibers to fill the cross-sectional area of a single voxel. Computationally, it is not possible to trace that many fibers. However, GO-ESP fiber tractography allows us to statistically represent the overall fiber distribution using unbiased sampling. To provide this unbiased sampling, GO-ESP generates the starting fiber positions r_0 using the equilibrium probability and the starting fiber orientations k_0 using the transition probability, and then produces an ensemble of fibers by integrating equation 2.1 with those initial conditions.

For each individual fiber traversing through any given voxel, an average fiber direction is estimated. Then the whole ensemble of fibers is used to calculate a total number of fibers and a mean direction of all fibers in every voxel. To construct a pairwise fiber crossing angle distribution in every voxel, we divide the range of all possible angles (from 0° to $\Theta=90^\circ$) into n bins and count the number of crossings N_{θ_i} falling in each bin i. Then we introduce a pairwise fiber crossing angle distribution density by normalizing it as

$$f(\theta) = \frac{nN_{\theta}}{N_{c}\Theta},\tag{2.4}$$

where N_c is a total number of crossings. This normalization ensures that

$$\int_{0}^{\Theta} f(\theta)d\theta = 1. \tag{2.5}$$

To illustrate the utility of this pairwise angle distribution, we first provide several simple examples showing how the density may look for simple geometric systems such as grid-like crossing of avenues and streets of Manhattan or curved streets of Victorian London.

Assuming that there is a family of N_f parallel fibers going through a single voxel gives us $N_c = N_f (N_f - 1)/2$ total crossings, all located at 0 degrees bin such that $f(0) = n/\Theta$, as shown in Figure 1A.

For two crossing families of parallel fibers (no necessarily orthogonal) with the same number of fibers N_f in each family, it will give $N_f(N_f-1)$ counts at 0 degrees bin and N_f^2 counts at the crossing angle θ_c bin (i.e., with $f(0) \approx f(\theta_c) \approx 0.5 n/\Theta$), as shown in Figure 1B.

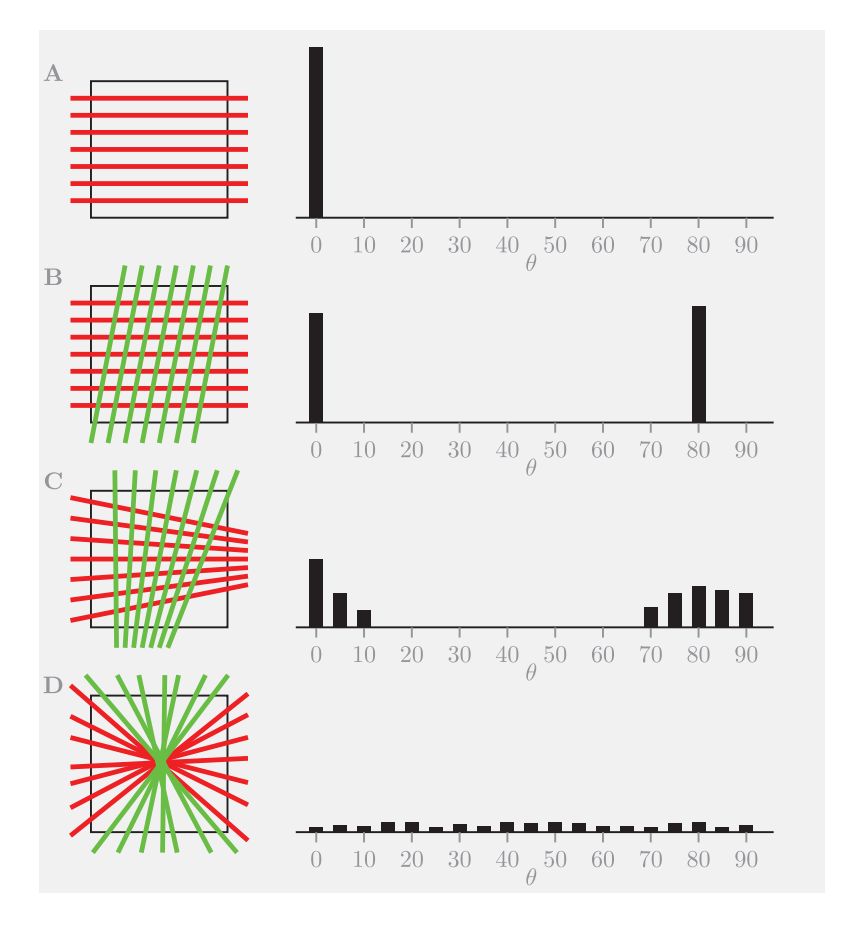


Figure 1: Several examples of idealized fiber distribution inside a voxel and an expected pairwise crossing fiber distribution density, including a single family of parallel fibers (A), two families of crossing parallel fibers (B), two families of crossing diverging fibers (C), and a random fiber distribution (D).

If both families of fibers are not strictly parallel but either diverging or converging (or just have some angular spread $\delta\theta$), their crossings will no longer be confined to two bins but instead will be spread out across the number of bins located in stripes with about $\delta\theta$ half-width adjacent to 0 degrees and θ_c bins. The crossing angle distribution density will roughly satisfy

$$\int_0^{\delta\theta} f(\theta)d\theta \approx \int_{\theta_c-\delta\theta}^{\theta_c+\delta\theta} f(\theta)d\theta \approx 0.5,$$

as shown in Figure 1C.

And finally, if there is no directional distinction between families of fibers or if some fiber directions are produced due to noise, then the number of crossings in each bin will follow the binomial distribution

$$P(N_{\theta}; N_{c}, p) = \frac{N_{c}!}{N_{\theta}!(N_{c} - N_{\theta})!} p^{N_{\theta}} (1 - p)^{(N_{c} - N_{\theta})},$$
(2.6)

where p = 1/n, giving

$$\mu_f = 1/\Theta, \qquad \sigma_f = \sqrt{(n-1)/N_c}/\Theta$$
 (2.7)

for the mean μ_f and the standard deviation σ_f of the crossing angle distribution density $f(\theta)$.

It is no surprise that the standard deviation σ_f is decreasing with the increase of number of crossings N_c as $1/\sqrt{N_c}$, as this is simply the restatement of the fact from elementary statistics that an error decreases as a square root of a number of trials. But this obvious fact allows us to show in the next section that the data with high statistical evidence prove that "the thesis that brain pathways adhere to a simple geometric system best accounts for the available evidence—not like London, but Manhattan" (Wedeen et al., 2012b) is is not supported in any way by the evidence provided by the data.

The main claim of Wedeen et al. (2012a) is that the white matter has a gridlike organization formed by crossing of quasi-orthogonal sheets of fibers. Though the crossing angles are not necessarily 90 degrees, they are nevertheless assumed to show some distinction between directions, which would translate into a pairwise crossing angle distribution containing peaks at both small and large angles. Our results do not find any quantitative statistical evidence that this is the case.

3 Results _

3.1 Pairwise Crossing Fiber Angle Distributions. To obtain the statistically relevant results, we generated up to 5 million seeds sampled from the unbiased equilibrium probability distribution generated by the ESP approach (Frank & Galinsky, 2014; Galinsky & Frank, 2015). Selecting approximately 2.5 million tracts of 60 mm length or longer and binning angles of all pairwise crossings of fibers in each voxel in the 0 to 90 degree range with 0.35 degree bin size produced the whole brain distribution shown as a stair-step graph in Figure 2A. The distribution includes more than 320,000 voxels where crossing of at least two fibers has been detected, with 1,722,128,284,856 fiber crossings total. It shows a relatively flat spread of crossing angles from rather low angles of about 10 degrees to the orthogonal crossing at 90 degrees. The number of crossings in the range from 80 degrees to 90 degrees corresponds to about 12% of all crossings, hence

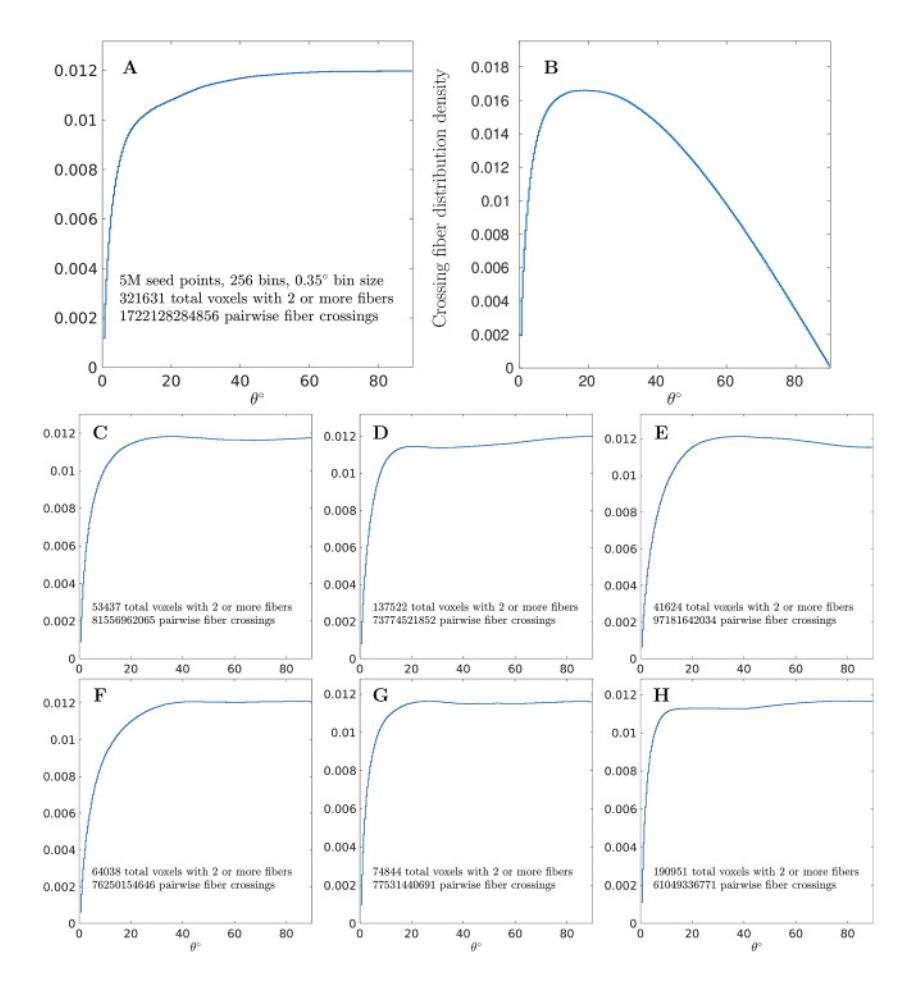


Figure 2: Pairwise crossing fiber angle distributions for the whole human brain. (A) Stair-step plot of distribution for 1,722,128,284,856 fiber crossings of MGH 1010 subject from the Human Connectome Project. The plot was obtained by selecting 2,494,224 fibers with 60 mm or more total length from the total of 5 million seed points and binning all pairwise angles θ from 321,631 voxels with two or more fibers in 256 bins of 0.35 degrees angular size. A fraction of fibers collected in each bin is shown on the ordinate axis. (B) Angle distribution rescaled by $\cos\theta$, which takes into account the difference in solid angle measures of each bin. Pairwise fiber angle distributions of six different subjects (C–H) scanned on different hardware (GE or Siemens) and processed with different parameters (including removing the restriction on fiber length, and changing the threshold to select different ranges of deep white matter) all show similar and repeatable whole brain pairwise crossing distributions.

shows the same trend as the significantly coarser results presented in the comment by Catani et al. (2012). The error bars in the stair-step graph of Figure 2A are not shown, as the total number of fiber crossings used for the binning of the whole brain pairwise angle distribution (about 1.7 trillion) provides an upper estimate for the error in the extremely low range of 10^{-6} .

If a random distribution of crossing angles in the azimuthal plane is assumed, then the difference in solid angle measure of bin sizes should be taken into account and used to scale the distribution with the cosine of the crossing angle θ . This distribution is shown in Figure 2B and provides the most likely angle for crossing fibers at only around 18 degrees.

Whole brain pairwise crossing fiber distributions for several additional subjects are shown in Figures 2C to 2H. These distributions were obtained using half a million seed points and varying parameters of GOESP tracking but keeping both initial seeding and all the tracking points in the deep white matter and the major tracts. It is believed that the deep white matter tracts is the primary focus of the Wedeen's paper, and it is at the crossings of the major white matter tracts where the so-called grid appears predominantly. For all six additional subjects in Figures 2C to 2H no large angle crossing peak was found, and all whole brain pairwise crossing distributions show a similar and rather repeatable form.

Several individual pairwise crossing angle distributions in selected voxels are shown in Figure 3. These distributions include a statistically evident single fiber, two crossing fibers, and multiple crossing fiber cases. All of these distributions use from about 8000 to 15,000 fibers to generate crossing angle distribution. The 10⁴ count of voxel fibers is of course nowhere close to about 10⁹ count of physical fibers, but nevertheless is high enough to provide sufficiently accurate and statistically significant results sampled from unbiased distribution with density represented by the equilibrium probability (Frank & Galinsky, 2014; Galinsky & Frank, 2015). These distributions also provide rather detailed information on the accuracy and resolution of our approach. For example, the single fiber distribution (see Figure 3A) shows an angular spread of only several degrees in a set of fibers bundled together. The two fibers crossing distribution (see Figure 3B) shows that our approach is capable of resolving fibers that cross with only around an 8 degree angle. Overall, the multitude of different crossing angle distributions can be spotted in different locations; examples of different crossings with about 20 degree, 45 degree and 90 degree angles are shown in Figures 3C, 3D, and 3E. Distributions with crossing of at least three sets of fibers are shown in Figures 3F and 3G, with evident peaks at both 45, and 80 degree angles. Even more complex distributions with multiple fibers are shown in the last two panels of Figure 3, where the last, Figure 3I again confirms that even for multiple fibers, our method is capable of finding fibers crossing with angles as small as only about 8 degrees.

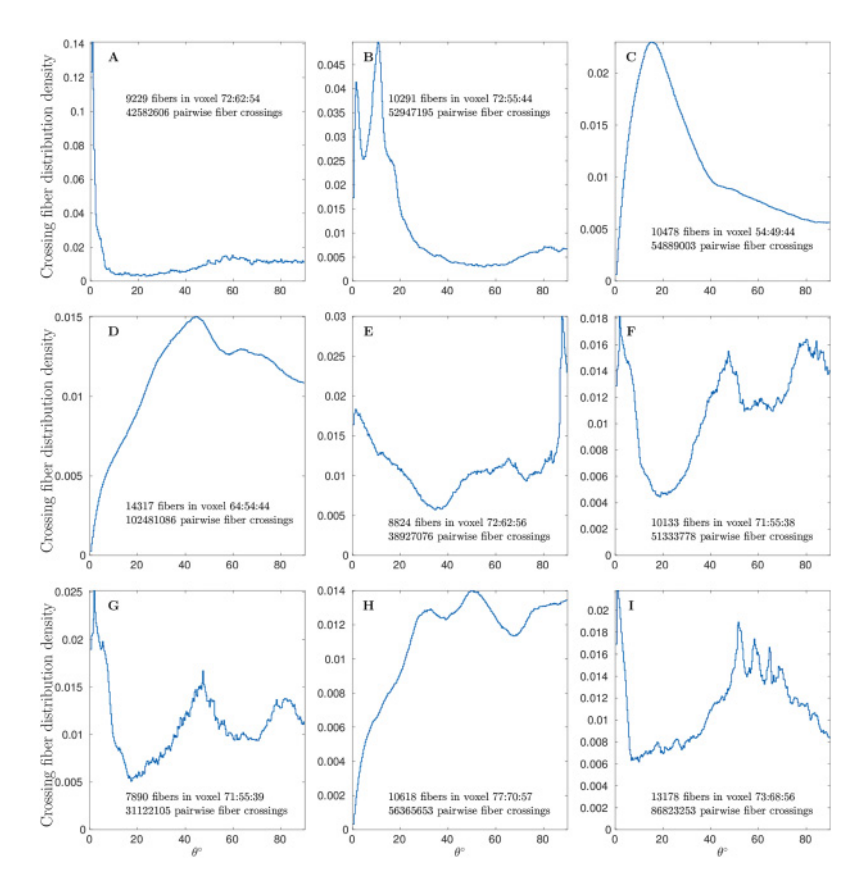


Figure 3: Pairwise crossing fiber angle distributions in several individual voxels showing examples of a single fiber (A), approximate 10, 20, 45, and 90 degrees crossing of two fibers (B, C, D, and E), and crossing of multiple fibers (F, G, H, and I).

3.2 Statistical Validation of Crossing Resolution. We emphasize that our claim of 8 degree resolution is very sound statistically. For example, with $N_f \sim 10^4$ fibers in Figure 3B, $N_c = N_f (N_f - 1)/2$ and about $\sim 5 \cdot 10^7$ total fiber crossings were used to generate the histogram. The 0.015 difference between the peak that represents the first family of fibers and the minimum that separates it from the second peak roughly corresponds to 600σ (σ is $\sim 2.4 \cdot 10^{-5}$ from 2.7). Even several peaks in the 50 degree to 70 degree range of Figure 3I (with as small as 0.001 height of the smallest peak) correspond to a range from 50σ to 150σ . While a more accurate significance estimate could be easily constructed from P-value bounds based on tail estimates for the binomial distribution itself, the normal approximation-based estimates

used here are more than sufficient to demonstrate the significance of the results.

The cumulative conditional probability of the hypothesis that the noise is responsible for formation of a peak N_{θ_1} relatively to a valley N_{θ_2} can be expressed as (Arratia and Gordon, 1989)

$$P_{v} = \sum_{N=N_{\theta_{1}}}^{N_{c}} \frac{P(N; N_{c}, p)}{P(N_{\theta_{2}}; N_{c}, p)} \lesssim \frac{1}{1 - r_{1}} \sqrt{\frac{N_{\theta_{2}}(N_{c} - N_{\theta_{2}})}{N_{\theta_{1}}(N_{c} - N_{\theta_{1}})}} e^{-N_{c}(H_{1} - H_{2})},$$
(3.1)

where

$$\begin{split} H(N_c, N_{\theta}, p) &= \frac{1}{N_c} \left[N_{\theta} \log \frac{N_{\theta}}{p N_c} + (N_c - N_{\theta}) \log \frac{N_c - N_{\theta}}{N_c (1 - p)} \right], \\ r_1 &= \frac{p(N_c - N_{\theta_1})}{(1 - p)N_{\theta_1}}, \quad H_1 \equiv H(N_c, N_{\theta_1}, p), \quad H_2 \equiv H(N_c, N_{\theta_2}, p). \end{split} \tag{3.2}$$

For the peak parameters of Figures 3B and 3I this expression results in extremely low P-values, as $H_1-H_2\sim 0.01$ and hence $\exp{(-0.01N_c)}$ dominates, giving the values that are slightly larger than $\operatorname{erfc}(600)$ for panel B or $\operatorname{erfc}(50)$ for panel I, but nevertheless well below the values considered reasonable by all current standards for successful statistical trials. This is clearly sufficient for validation of approximately 8 degrees as the resolution of our approach.

3.3 Crossing Examples with Locations and Directional Maps. Figure 4 shows 3D views of a subset of randomly selected fibers for voxels from panels B, C, D, and F of Figure 3. Low-resolution and high-resolution videos can be accessed through the online supplement links.

Locations of the voxels on two-dimensional slices of the MGH 1010 T1 volume are shown in Figure 5. The parula-colored overlay shows the map of fiber counts in every voxel of the slice. It can be clearly seen that the fibers used for our analysis are located in the areas of deep white matter and major tracts, hence directly correspond to the area that is the primary focus of Wedeen et al. (2012a).

The directional information for several selected slices is shown in Figure 6. The figure includes panels A, C, and E with two-dimensional slices of MGH 1010 T1 volume overlaid by an RGB map of the major eigenvector of the transition probabilities (Galinsky & Frank, 2015) calculated from volumetric diffusion data and used as priors in seeding of the tracts. The second set of panels, B, D, and F, looks only slightly different visually, but it is based on a conceptually different analysis. RGB directional maps

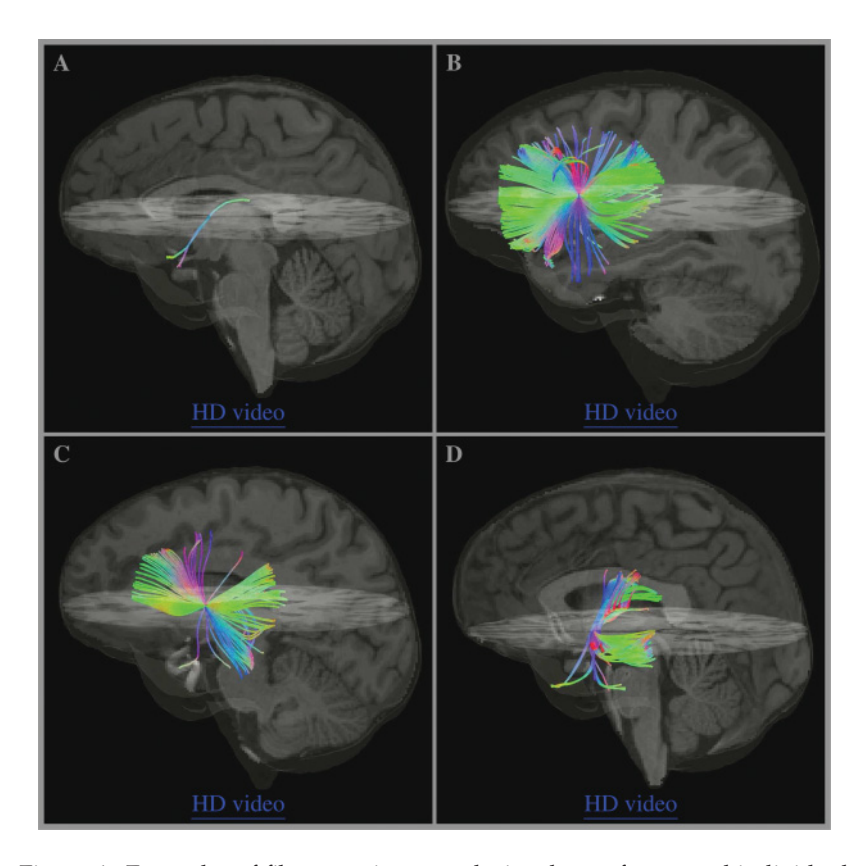


Figure 4: Examples of fiber crossing complexity shown for several individual voxels with pairwise crossing fiber angle distributions in Figure 3. Panels **A**, **B**, **C**, **and D** correspond to panels **B**, **C**, **D**, **and F**, respectively, showing a subset of 201, 268, 487, and 157 randomly selected fibers (out of 10,291, 10,478, 14,317, and 10,133 total fibers used in Figure 3). Low-resolution, high-resolution videos can be accessed through video links presented in the online supplement available at http://www.mitpressjournals.org./doi/suppl/10.1162/NECO_a_00896.

are produced from an ensemble of curved line tracts obtained by our GO-ESP approach and postprocessed to generate the mean fiber directions for each voxel using the procedure described in section 2.

Panels A, B, C, and D of Figure 6 also include the location of the same four voxels marked by labels in Figure 5. Even the voxels that seem to be located deep inside the areas of predominantly single color, that is, with the same major directions of transitional probabilities or the same averaged direction of all fibers (i.e., voxels labeled as A and C), correspond to rather complicated crossing structures, as can be seen from 3D views and videos of Figure 4.

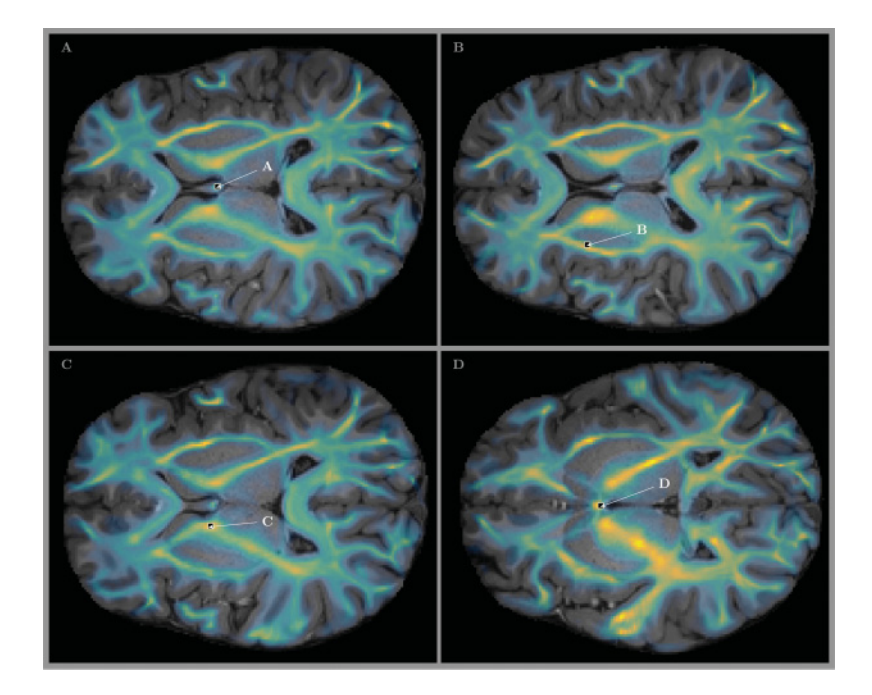


Figure 5: Locations of the voxels shown in **A**, **B**, **C**, and **D** of Figure 4 and in **B**, **C**, **D**, and **F** panels of Figure 3. The parula-colored overlay shows the map of fiber counts across the slices. It can be clearly seen that the fibers used for our analysis are located in the areas of deep white matter and major tracts, the primary focus of Wedeen et al. (2012a).

Another set of individual pairwise crossing angle distributions from a contiguous block of 3×3 voxels is shown in Figure 7. The set clearly indicates continuity of the distribution across voxel boundaries with small consistent changes from voxel to voxel. An abundance of various angles of crossing fibers from $\lesssim 20$ to 90 degrees is also evident in each of these adjacent voxels.

The position of this block of 3×3 voxels is shown in panel A of Figure 8. For comparison, panel B shows (by label E) the location of a relatively neighboring voxel where the only histogram has been spotted (see Figure 3E) that resembles the crossing sheet structure expected to be common in the deep white matter and major tracts area according to the claims by Wedeen et al. (2012a).

Several more examples of fiber tracts crossing in different areas of different subjects are shown in Figure 11 in the appendix, again with low-resolution and high-resolution videos accessible through the online supplemental links. The overall fiber tracts structure seems to be more

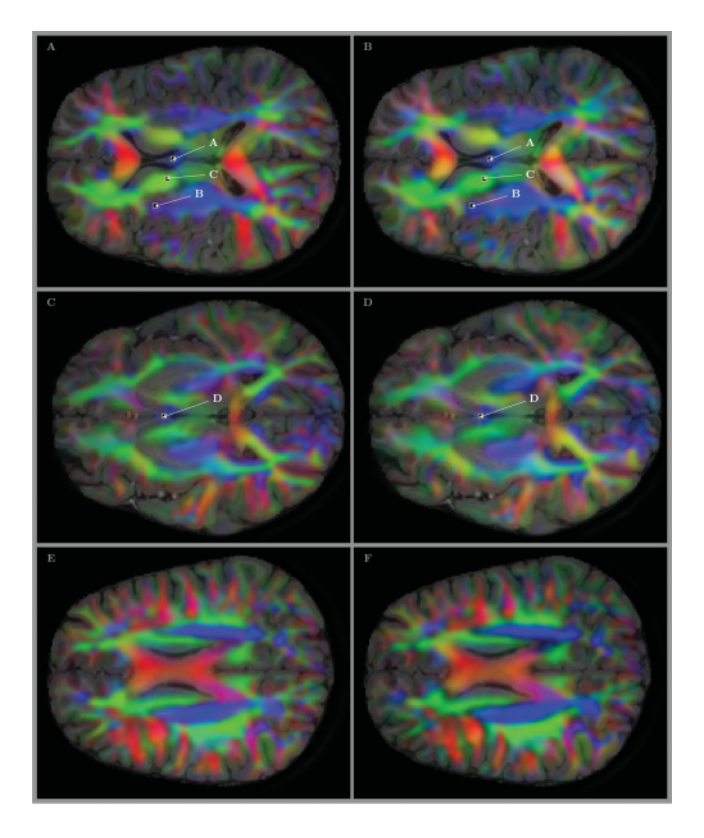


Figure 6: Locations of the voxels shown in **A**, **B**, **C**, and **D** of Figures 4 and 5 and panels in **B**, **C**, **D**, and **F** of Figure 3. The RGB-colored overlays show the directional information for the transition probabilities (Galinsky & Frank, 2015) used in seeding (panels A, C, and E) and for the mean fiber directions obtained by our analysis as a result of processing an ensemble of tracts in every voxel (panels B, D, and F). All four voxels marked by labels inside the panels show rather complicated crossing structures, even those located deep in areas of predominantly common colors—that is, with the same major directions of transitional probabilities or mean fiber directions (i.e., voxels labeled as A and C).

consistent with small angle treelike branching of tracts rather than with near-orthogonal gridlike crossing of fiber sheets. Treelike branching structures are well known in neuronal growth, and their existence has been posited on a range of evolutionary factors (Mitchison, 1991; Laughlin & Sejnowski, 2003; Sugimura, Shimono, Uemura, & Mochizuki, 2007; Wen, Stepanyants, Elston, Grosberg, & Chklovskii, 2009; Jan & Jan, 2010; Gibson & Ma, 2011). Our finding of this structure on the macro (brain) scale, while remarkable, is thus perhaps not surprising in light of this similarity

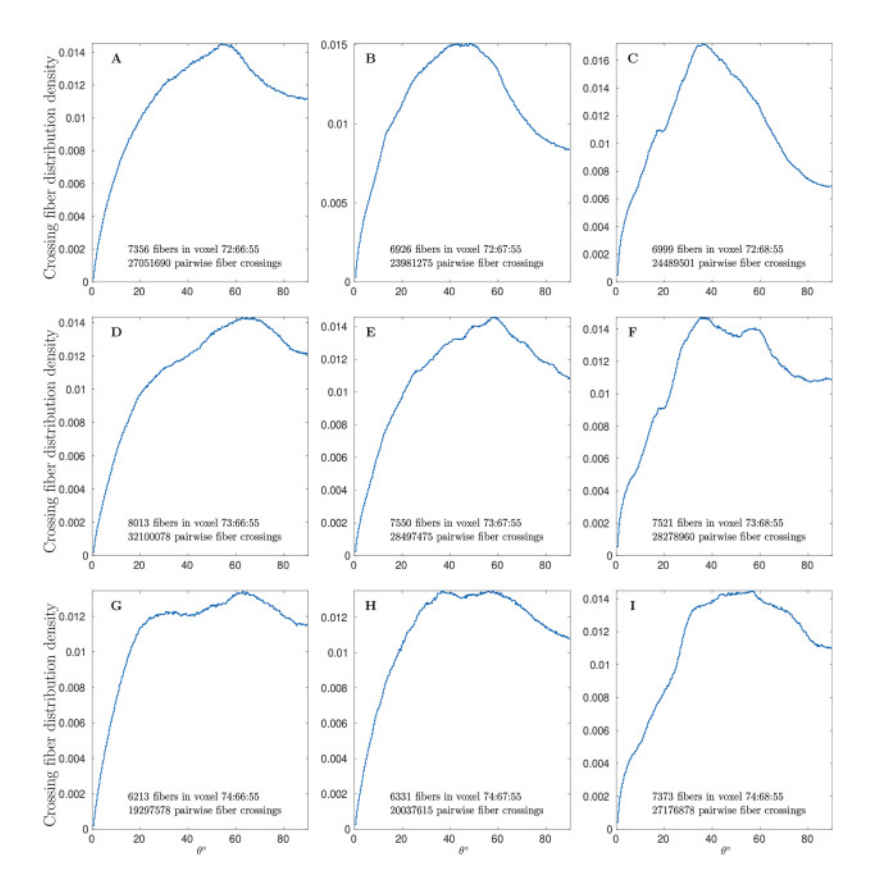


Figure 7: Pairwise crossing fiber angle distributions in a 3×3 block of adjacent voxels showing the continuity of distributions across voxel boundaries. The fraction of fiber crossings in the voxel is shown on the ordinate axis.

to the microscale (neuronal) geometry, as well as the proliferation of such structures in complex biological systems (Ochoa-Espinosa & Affolter, 2012).

3.4 The Lamellar Structure of Fiber Pathways. The capabilities of our GO-ESP method for constructing accurate quantitative measures of complex fiber distributions, as demonstrated above, provide a unique opportunity to investigate the possibility of a quantitative measure of the geometrical structure of brain fibers. One such measure became apparent in our recent investigations and is shown in Figure 9, where we have plotted fiber pathways colored by the direction of the local vorticity $\omega = \nabla \times v \equiv \operatorname{rot}(v)$. For the v field, we use $\psi(r,k)$ (see equation 2.1; Galinsky & Frank, 2015, for details) with k fixed for a given family of fibers at location r. It is well known from vector calculus that the extreme case

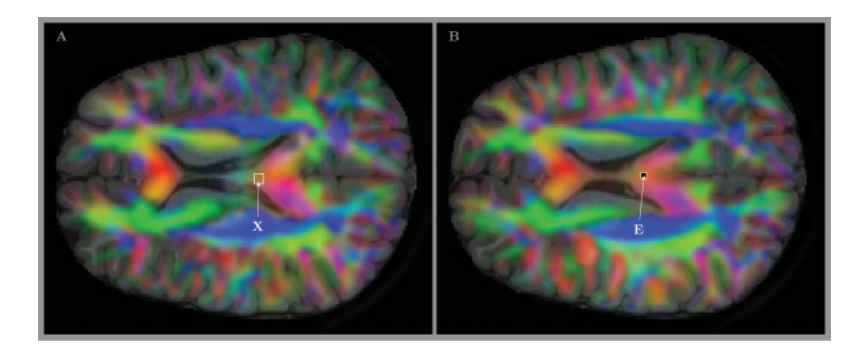


Figure 8: T1 images with the RGB-colored directional information for the mean fiber direction used to show the position of 3×3 block of voxels from Figure 7 (small rectangle X in panel A) and the location of relatively neighboring voxel where the only histogram was identified (see Figure 3E) that resembles the crossing sheet structure expected to be common in the deep white matter and major tracts area according to the claims by Wedeen et al. (2012a) (label E in panel B).

of a vector field orthogonal to its own vorticity (i.e., when $\mathbf{v} \cdot \nabla \times \mathbf{v} = 0$) is called a lamellar vector field. The opposite extreme case of vorticity parallel to the field, (i.e., when $\mathbf{v} \times \nabla \times \mathbf{v} = 0$) is known as a helical vector field. Since no experimentally measured fiber vorticity fields would be expected to satisfy either of these cases identically, it nevertheless makes sense to consider approximate lamellar and helical conditions. In Figure 9A only those parts of fibers in color that satisfy the approximately lamellar condition $|\mathbf{v} \cdot \boldsymbol{\omega}|/|\mathbf{v}||\boldsymbol{\omega}| < \sqrt{2}/2$. The approximately helical condition $|\mathbf{v} \cdot \boldsymbol{\omega}|/|\mathbf{v}||\boldsymbol{\omega}| > \sqrt{2}/2$ is used for coloring in Figure 9B. The same coloring is used for several cuts through the brain with horizontal, coronal, and sagittal planes in Figure 10. Comparing Figure 9A with Figure 9B (and Figure 10A with Figure 10B), it is strikingly obvious that the brain fiber pathways, although neither strictly lamellar nor strictly helical, show very significant prevalence of lamellarity over helicity. An important mathematical property of the lamellar field is the existence of Monge decomposition of vector field $v = \lambda \nabla \mu$, such that there exists a set of equipotential surfaces $\mu = \text{const}$ orthogonal to vector field lines (fiber tracts) everywhere (Lamb, 1932; Serrin, 1959). This propensity for lamellarity in human brain fiber pathways is an interesting fact that clearly warrants a more in-depth investigation. However, the strong prevalence for global lamellarity in the brain fiber pathways demonstrated in this letter at least suggests a plausible quantitative connection between structure and evolution that is consistent with the ubiquity of lamellar structures in biological systems (Fernández-Morán, 1959; Weiner, Addadi, & Wagner, 2000).

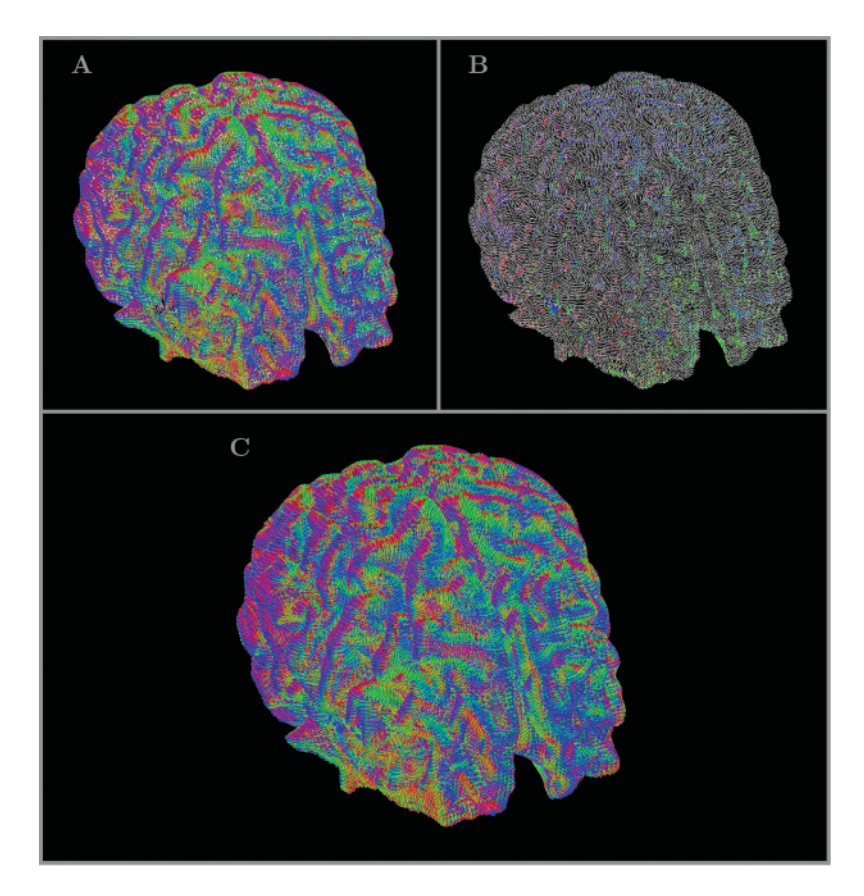


Figure 9: Lamellar (A) and helical (B) parts of the brain fiber pathways colored with the unit vector of the local vorticity $\omega/|\omega|$ (C).

4 Discussion and Conclusion _____

The identification of sheet structures in the brain from DTI data requires two quantitative steps. The first is the ability to accurately estimate intravoxel fiber distributions from DTI data. The second is the development of a quantitative characterization of sheet structures. However, the ability to perform the second step is predicated on being able to perform the first. Without an accurate estimation of the intravoxel fiber distribution, any statements about sheet structure, however they are formulated, will be relatively meaningless.

This major limitation of current DTI analysis methods motivated our development of the GO-ESP method used in this letter, which has been demonstrated to overcome many of these limitations and provides a robust method for the accurate (to within image resolution) estimation of the local

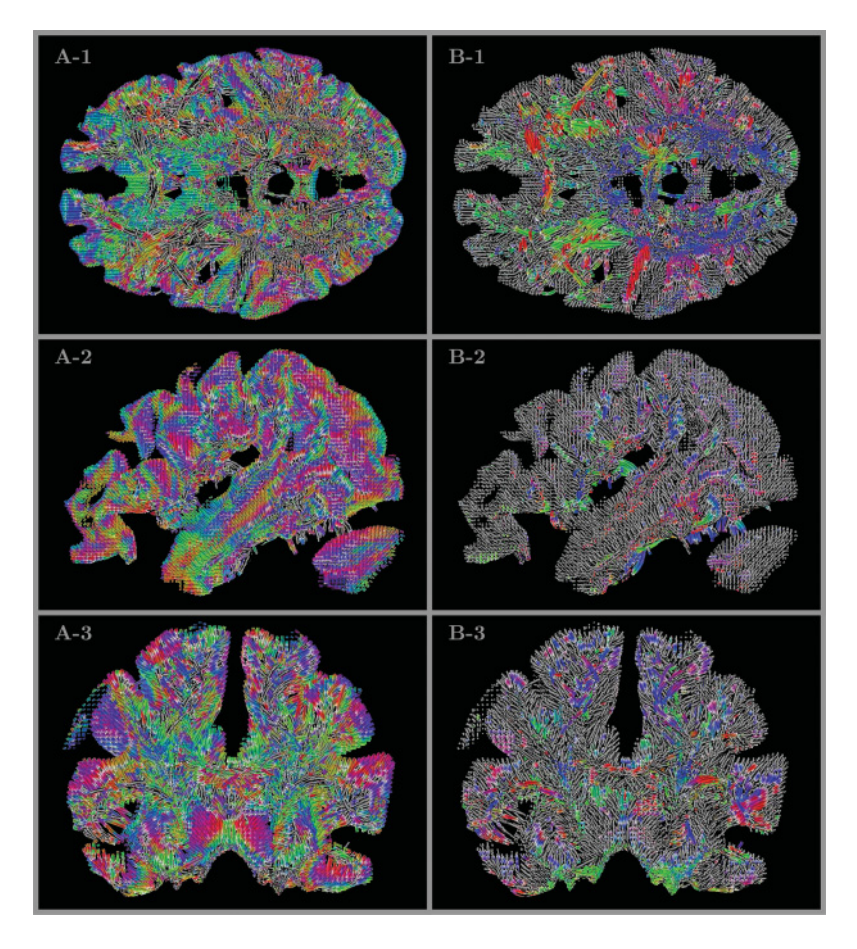


Figure 10: Lamellar (A) and helical (B) parts of the brain fiber pathways colored with the unit vector of the local vorticity $\omega/|\omega|$ and shown using horizontal (1), coronal (2), and sagittal (3) cuts of the brain.

diffusion profile (Galinsky & Frank, 2015). This is the first novel aspect of the our study. In addition, we have developed a robust statistical assessment of the existence of sheet structures based on intravoxel pairwise fiber crossing distributions. The original conclusions of Wedeen et al. (2012a) were based a nonquantitative visual assessment of intervoxel fiber relationships. In a recent series of abstracts, Tax and colleagues entered this debate by aiming to more quantitatively describe sheet structures from intervoxel structure using well-known differential geometric methods (Tax et al., 2013, 2014, 2015, Tax, Haije, 2016; Tax Westin, et al., 2016). Unfortunately, their approach is incapacitated by their reliance on standard DTI analysis

methods, which are incapable of accurately discerning intravoxel distributions, thus requiring, for example, the invocation of artificial methods to account for the missing peaks in their characterization of the local diffusion by a fiber orientation distribution function (fODF) (Tax, Westin, et al., 2016).

On the contrary, our approach is more in the spirit of the fiber angle distributions of Catani et al. (2012), with the significant improvements that we employ a method that can robustly estimate intravoxel fiber orientation probabilities (Galinsky & Frank, 2015), from which we then construct quantitative statistical assessments of the relationship of intravoxel fiber distributions to sheet structures. These assessments are not based on any assumption of orthogonality (see Figure 1C) but rather on the statistical distributions expected from sheet structures. Within the spatial resolution limits, our assumption of noncurved fibers within a single voxel implicit in our formulation of the intravoxel sheet distributions is sufficiently accurate, and there is no need to invoke any differential geometric machinery that might be required for considering intervoxel fiber architectures. In addition, we have demonstrated that there is, in fact, a concise global (i.e., intervoxel) mathematical characterization of the brain fiber architecture as a lamellar vector field.

The general conclusion of our study is that our results provide no quantitative statistical evidence for the model of brain fiber architecture as crossing sheets of fibers postulated by Wedeen et al. (2012a) locally, in many of the individual voxels, and globally, statistically averaging all crossings of fibers in the whole brain. Nevertheless, the question of whether there is a quantitative measure of the geometrical structure of brain fibers is very important for understanding the development and function of the human brain. Our findings provide interesting insight into a possible approach to the development of such a quantitative measure by showing significant prevalence of lamellarity over helicity across the whole ensemble of brain fibers.

It is useful here to summarize our approach and the major results of this study. We analyzed whole brain tractography results for several subjects and introduced a pairwise fiber crossing angle distribution with small angular bin (as small as only 0.35 degrees). Using a large number of tracks allowed us to draw statistically significant conclusions from those distributions even on the scale of a single voxel. We showed that our method is capable of capturing with high statistical certainty crossing of bundles or sheets or planes at angles below 10 degrees. We showed that crossing of two bundles or sheets of divergent fibers would be expected to produce two peaks in the distribution. Similarly, for fibers confined to three crossing planes in 3D volume, the expectation would be to find either three or two clearly defined peaks. However, our results demonstrate a much wider range of possible crossing configurations, from just a single divergent bundle of fibers to crossing of fibers coming from more than three clearly defined directions (i.e., crossing of more than three planes in a single voxel) and thus suggest a much more complex overall picture of the

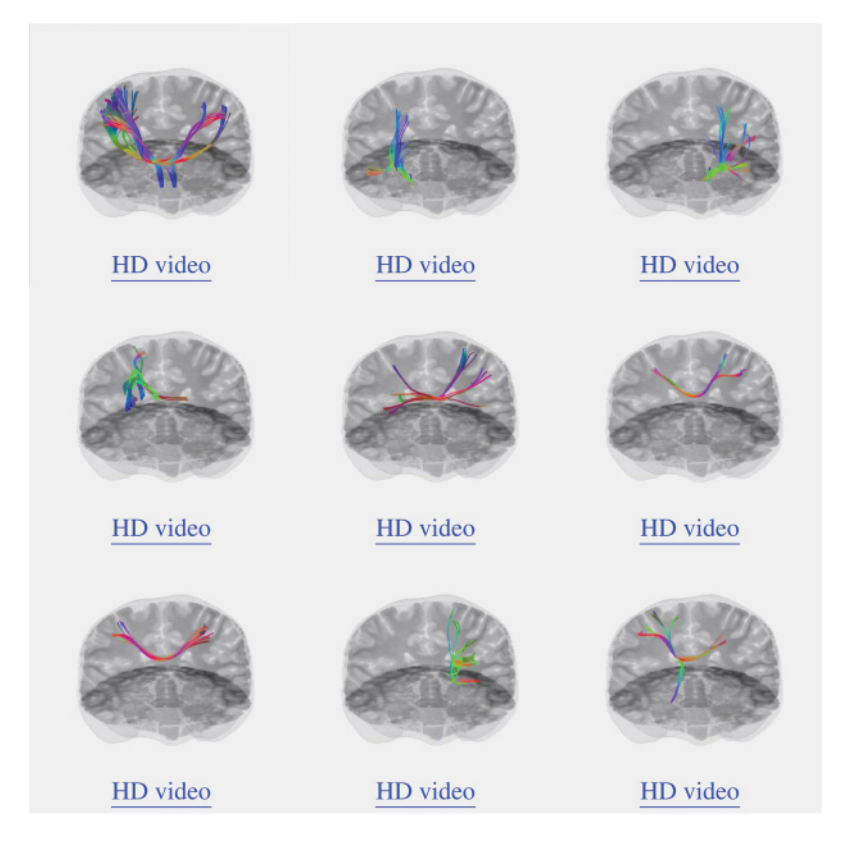


Figure 11: Examples of crossing fibers. Video clips for high definition are in the online supplement.

brain fiber architecture. A significant finding of our study is that there does indeed appear to be evidence for an underlying structure of the brain fibers: they form a lamellar vector field. This property is much more complex than the simple crossing of three curved coordinate planes (either orthogonal or not) Wedeen et al. (2012a, 2012b) claimed. And yet it is expressible in a concise and unambiguous mathematical form and is numerically demonstrable on real data, as we have done by showing the significant prevalence of lamellarity over helicity.

Appendix: Fiber Crossing Examples ___

More examples of fiber crossings from different subjects are provided in Figure 11. Low-resolution and high-resolution videos can be accessed through the online supplement.

Acknowledgments _

L.R.F. and V.L.G. were supported by NSF grants DBI-1143389, DBI-1147260, EF-0850369, PHY-1201238 and NIH grant R01 MH096100. We thank Alec Wong and Tom Liu at the UCSD CFMRI and Scott Sorg at the VA San Diego Health Care System for providing the diffusion-weighted imaging data. Data were provided in part by the Human Connectome Project, WU-Minn Consortium (principal investigators David Van Essen and Kamil Ugurbil; 1U54MH091657) funded by the 16 NIH institutes and centers that support the NIH Blueprint for Neuroscience Research; and by the McDonnell Center for Systems Neuroscience at Washington University. Data collection and sharing for this project were provided by the Human Connectome Project (HCP; principal investigators Bruce Rosen, Arthur W. Toga, and Van J. Weeden). HCP funding was provided by the National Institute of Dental and Craniofacial Research, the National Institute of Mental Health, and the National Institute of Neurological Disorders and Stroke. HCP data are disseminated by the Laboratory of Neuro Imaging at the University of Southern California.

References

- Arratia, R., & Gordon, L. (1989). Tutorial on large deviations for the binomial distribution. *Bull. Math. Biol.*, *51*(1), 125–131.
- Basser, P. J., Pajevic, S., Pierpaoli, C., Duda, J., & Aldroubi, A. (2000). In vivo fiber tractography using DT-MRI data. *Magn. Reson. Med.*, 44(4), 625–632.
- Catani, M., Bodi, I., & Dell'Acqua, F. (2012). Comment on "The Geometric Structure of the Brain Fiber Pathways," *Science*, 337, 1605. doi:10.1126/science.1223425
- Christiaens, D., Reisert, M., Dhollander, T., Sunaert, S., Suetens, P., & Maes, F. (2015). Global tractography of multi-shell diffusion-weighted imaging data using a multi-tissue model. *Neuroimage*, 123, 89–101.
- Conturo, T. E., Lori, N. F., Cull, T. S., Akbudak, E., Snyder, A. Z., Shimony, J. S., ... Raichle, M. E. (1999). Tracking neuronal fiber pathways in the living human brain. *Proc. Natl. Acad. Sci. U.S.A.*, *96*(18), 10422–10427.
- Fernández-Morán, H. (1959). Fine structure of biological lamellar systems. *Reviews of Modern Physics*, 31(2), 319–330.
- Fillard, P., Poupon, C., & Mangin, J. F. (2009). A novel global tractography algorithm based on an adaptive spin glass model. *Med. Image. Comput. Comput. Assist. Interv.*, 12(Pt. 1), 927–934.
- Frank, L. R., & Galinsky, V. L. (2014). Information pathways in a disordered lattice. *Phys. Rev. E*, 89, 032142.
- Galinsky, V. L., & Frank, L. R. (2015). Simultaneous multi-scale diffusion estimation and tractography guided by entropy spectrum pathways. *IEEE Trans. Med. Imaging*, 34(5), 1177–1193.
- Gibson, D. A., & Ma, L. (2011). Developmental regulation of axon branching in the vertebrate nervous system. *Development*, 138(2), 183–195.

- Goh, A., Lenglet, C., Thompson, P. M., & Vidal, R. (2009). Estimating orientation distribution functions with probability density constraints and spatial regularity. *Med. Image Comput. Comput. Assist. Interv.*, 12(Pt. 1), 877–885.
- Jan, Y. N., & Jan, L. Y. (2010). Branching out: Mechanisms of dendritic arborization. *Nature Reviews Neuroscience*, 11(5), 316–328.
- Jbabdi, S., & Johansen-Berg, H. (2011). Tractography: Where do we go from here? *Brain Connect.*, 1(3), 169–183.
- Keil, B., Blau, J. N., Biber, S., Hoecht, P., Tountcheva, V., Setsompop, K., & Wald, L. L. (2013). A 64-channel 3T array coil for accelerated brain MRI. Magnetic Resonance in Medicine, 70(1), 248–258. doi:10.1002/mrm.24427
- Kreher, B. W., Schnell, S., Mader, I., Il'yasov, K. A., Hennig, J., Kiselev, V. G., & Saur, D. (2008). Connecting and merging fibres: Pathway extraction by combining probability maps. *Neuroimage*, 43(1), 81–89.
- Lamb, H. (1932). Hydrodynamics. New York: Dover.
- Laughlin, S. B., Sejnowski, T. J. (2003). Communication in neuronal networks. *Science*, 301(5641), 1870–1874.
- Mitchison, G. (1991). Neuronal branching patterns and the economy of cortical wiring. *Proceedings of the Royal Society of London B: Biological Sciences*, 245(1313), 151–158.
- Mori, S., & van Zijl, P. C. (2002). Fiber tracking: Principles and strategies—a technical review. *NMR Biomed.*, 15(7–8), 468–480.
- Ochoa-Espinosa, A., & Affolter, M. (2012). Branching morphogenesis: From cells to organs and back. *Cold Spring Harbor Perspectives in Biology*, 4(10), 1–14.
- Reisert, M., Kiselev, V. G., Dihtal, B., Kellner, E., & Novikov, D. S. (2014). MesoFT: Unifying diffusion modelling and fiber tracking. *Med. Image Comput. Comput. Assist. Interv.*, 17(Pt. 3), 201–208.
- Reisert, M., Mader, I., Anastasopoulos, C., Weigel, M., Schnell, S., & Kiselev, V. (2011). Global fiber reconstruction becomes practical. *Neuroimage*, 54(2), 955–962.
- Serrin, J. (1959). Mathematical principles of classical fluid mechanics. *Handbuch der Physik*, 8, 125–263. doi:10.1007/978-3-642-45914-6_2
- Setsompop, K., Gagoski, B. A., Polimeni, J. R., Witzel, T., Wedeen, V. J., & Wald, L. L. (2011). Blipped-controlled aliasing in parallel imaging for simultaneous multislice echo planar imaging with reduced g-factor penalty. *Magn. Res. Med.*, 67(5), 1210–1224.
- Setsompop, K., Kimmlingen, R., Eberlein, E., Witzel, T., Cohen-Adad, J., Mc-Nab, J., & Wald, L. (2013). Pushing the limits of in vivo diffusion (MRI) for the human connectome project. *NeuroImage*, 80(0), 220–233. doi: 10.1016/j.neuroimage.2013.05.078
- Sotiropoulos, S. N., Moeller, S., Jbabdi, S., Xu, J., Andersson, J. L., Auerbach, E. J., & Lenglet, C. (2013). Effects of image reconstruction on fiber orientation mapping from multichannel diffusion MRI: Reducing the noise floor using sense. *Magnetic Resonance in Medicine*, 70(6), 1682–1689. doi:10.1002/mrm.24623
- Sugimura, K., Shimono, K., Uemura, T., & Mochizuki, A. (2007). Self-organizing mechanism for development of space-filling neuronal dendrites. *PLoS Comput. Biol.*, *3*(11), e212.

- Tax, C., Haije, T. D., Fuster, A., Duits, R., Viergever, M., Calabrese, E., & Leemans, A. (2015). Towards quantification of the brain's sheet structure in diffusion MRI data. In *Proceedings of the International BASP Frontiers Workshop*, (p. 74).
- Tax, C., Haije, T. D., Fuster, A., Duits, R., Viergever, M., Florack, L., & Leemans, A. (2014). Towards quantification of the brain's sheet structure: Evaluation of the discrete Lie bracket. In *Proceedings of the International Society Magnetic Resonance in Medicine*, (p. 0975).
- Tax, C., Haije, T. D., Fuster, A., Viergever, M., Florack, L., & Leemans, A. (2013). Considerations on the theory of sheet structure of cerebral pathways. In *Proceedings of the ISMRM Workshop on Diffusion as a Probe of Neural Tissue Microstructure*.
- Tax, C., Haije, T. D., Fuster, A., Westin, C. F., Viergever, M., Florac, L., & Leemans, A. (2016). Mapping the brain's sheet probability index (SPI) with diffusion MRI: Sheet happens?! In *Proceedings of the International Society Magnetic Resonance in Medicine*, (p. 791).
- Tax, C., Westin, C. F., Haije, T. D., Fuster, A., Viergever, M., Florac, L., & Leemans, A. (2016). Robust assessment of the brain's sheet structure using normalized convolution. In *Proceedings of the International Society Magnetic Resonance in Medicine*, (p. 2073).
- Tournier, J. D., Calamante, F., & Connelly, A. (2007). Robust determination of the fibre orientation distribution in diffusion MRI: Non-negativity constrained superresolved spherical deconvolution. *NeuroImage*, 35(4), 1459–1472.
- Tuch, D., Reese, T., Wiegell, M., Makris, N., Belliveau, J., & Wedeen, V. (2002). High angular resolution diffusion imaging reveals intravoxel white matter fiber heterogeneity. Magn. Reson. Med., 48, 577–582.
- Van Essen, D. C., Ugurbil, K., Auerbach, E., Barch, D., Behrens, T. E., Bucholz, R., & Yacoub, E. (2012). The Human Connectome Project: A data acquisition perspective. NeuroImage, 62(4), 2222–2231.
- Wedeen, V. J., Rosene, D. L., Wang, R., Dai, G., Mortazavi, F., Hagmann, P., & Tseng, W. Y. I. (2012). The geometric structure of the brain fiber pathways. *Science*, 335, 1628. doi:10.1126/science.1215280
- Wedeen, V. J., Rosene, D. L., Wang, R., Dai, G., Mortazavi, F., Hagmann, P., & Tseng, W. Y. I. (2012). Response to comment on "The Geometric Structure of the Brain Fiber Pathways". Science, 337, 1605. doi:10.1126/science.1223493
- Wedeen, V. J., Wang, R. P., Schmahmann, J. D., Benner, T., Tseng, W. Y., Dai, G., & de Crespigny, A. J. (2008). Diffusion spectrum magnetic resonance imaging (DSI) tractography of crossing fibers. *NeuroImage*, 41(4), 1267–1277.
- Weiner, S., Addadi, L., & Wagner, H. D. (2000). Materials design in biology. *Materials Science and Engineering: C*, 11(1), 1–8.
- Wen, Q., Stepanyants, A., Elston, G. N., Grosberg, A. Y., & Chklovskii, D. B. (2009). Maximization of the connectivity repertoire as a statistical principle governing the shapes of dendritic arbors. *Proceedings of the National Academy of Sciences of the United States of America*, 106(30), 12536–12541.